Pol. J. Environ. Stud. Vol. XX, No. X (XXXX), 1-14
DOI: *10.15244/pjoes/214081* ONLINE PUBLICATION DATE: 2026-02-18

Original Research

Efficient Removal of Sb(III) Using Fe-Mn-Modified Wheat Straw Biochar: Multifaceted Optimization and Mechanism

Guangzheng Zhou, Jia Lu, Ning Liu, Dun Fu°*

Key Laboratory of Coalbed Methane Development and Mining Area Environmental Remediation of Suzhou City, School of Resources and Civil Engineering, Suzhou University, Suzhou 234000, Anhui, China

Received: 31 July 2025
Accepted: 08 November 2025

Abstract

In this study, wheat straw was used as a raw material to prepare biochar (BC), and an in situ impregnation and carbonization method was adopted to prepare Fe-Mn-modified BC (FMBC) composites for the adsorption of antimonite (Sb(III)) in water. Adsorption kinetics, response surface curves, and isothermal adsorption were utilized to conduct in-depth research on the adsorption performance of FMBC for removing antimony in water. Modern characterization techniques such as X-ray diffraction, Fourier transform infrared spectroscopy, scanning electron microscopy, transmission electron microscopy, and X-ray photoelectron spectroscopy (XPS) were used to investigate the mechanism of antimony adsorption from water by FMBC. Results showed that FMBC had stronger adsorption performance for Sb(III) than wheat straw BC, with the maximum adsorption amount of 23.76 $mg \cdot g^{-1}$ at 35°C. In the kinetic experiments, the quasi-secondary kinetic model could efficiently describe the whole adsorption process, which indicated that the adsorption process was mainly dominated by chemisorption. After the response surface optimization, the removal rate of Sb(III) could reach 93.73% under optimal conditions. The results of isothermal adsorption experiments showed that the adsorption process was considerably in line with the Langmuir model, indicating that this adsorption was inclined to monomolecular-layer adsorption. XPS and other analyses demonstrated that FMBC mainly consisted of iron oxides and manganese oxides and had a large specific surface area, with an abundance of oxygen-containing functional groups. The mechanism of Sb(III) adsorption by FMBC primarily comprised redox reactions, complexation, and ion exchange. The above results indicated that the Fe–Mn-modified wheat straw BC could be used as an effective adsorption material for the treatment of Sb(III)-containing wastewater.

Keywords: iron-manganese-modified biochar, antimonite adsorption, response surface optimization, adsorption-oxidation mechanism

*e-mail: fudun@ahszu.edu.cn
°ORCID iD: 0000-0001-8884-1119

Introduction

With the vigorous development of industrialization and the acceleration of urbanization, the problem of heavy metal pollution in water bodies has gradually come to the forefront and has become a major problem that needs to be solved [1]. Antimony is toxic and widely found in the natural environment and industrial wastewater [2]. During the evolution of the natural environment, antimony gradually migrates to water bodies through soil, rocks, and other media [3, 4]. Antimony-containing wastewater is generated during industrial production activities such as textile printing and dyeing and metal smelting [5]. Sb exists in the aqueous environment mainly in the form of antimonite (Sb(III)) and antimonate (Sb(V)), with the toxicity of Sb(III) being approximately 10 times that of Sb(V) [6]. The European Union and the U.S. Environmental Protection Agency listed antimony as a priority control pollutant in 1976 and 1979, respectively, and stipulated that the content in drinking water should not exceed 5 and 6 μg L^{-1}, respectively [7]. In recent years, China's antimony wastewater discharge standards have become increasingly stringent, and enterprises involved in antimony are facing severe challenges; therefore, a low-cost and highly efficient technology for the removal of heavy metals in antimony-containing wastewater should be explored urgently [8, 9].

Current technologies for treating antimony-containing wastewater mainly include chemical reduction [10], ion exchange [11], adsorption [12], and membrane separation [13]. In the adsorption method, the target pollutant is adsorbed to the surface of the adsorbent through the physicochemical adsorption between the adsorbent and adsorbate, then solid–liquid separation is performed to achieve the goal of removing the pollutant [14]. This method has many advantages, such as low cost, high selectivity, easy operation, and a renewable adsorbent, and has gradually become one of the most widely used and effective methods for the treatment of water pollutants [15]. Biochar (BC), as a carbonaceous material made by the pyrolysis of biomass at high temperatures, has a porous structure, high specific surface area, and good chemical stability and has been widely used in soil improvement, environmental remediation, and energy fields [16]. In actual wastewater, because of the coexistence of multiple heavy metals or the high content of heavy metals, the adsorption performance of BC on them is poor, or costly material investment is required; thus, the appropriate raw material selection and BC modification are effective ways to improve the adsorption performance [17].

Wheat straw, as an agricultural waste, can be recycled and transformed into a green resource for biochar preparation; this technique benefits from simple operation and readily available materials [18]. As a byproduct of global staple crop production, its annual output exceeds one billion tons, ensuring stable and sustainable availability. Its growth follows the natural carbon cycle of photosynthesis (typically ≤1 year), aligning with the carbon neutrality principles. Furthermore, its acquisition cost is significantly lower than conventional adsorbents, being only 1/5 to 1/3 of the latter (approximately 200-500 CNY per ton), demonstrating notable dual advantages in both the economic and environmental aspects. However, the adsorption capacity of virgin BC for specific heavy metals is limited, and it needs to be modified to improve its adsorption performance [19]. Currently, BC modification is mostly based on metal oxides such as nickel [20], cobalt [21], iron, and manganese [22, 23], which are used to adsorb heavy metals in wastewater. For instance, Wu et al. [24] developed a novel zero-valent iron-modified biochar beads (PEI/SA/BCFe), achieving a remarkable Sb(III) adsorption capacity of 621.04 mg g^{-1} at 10°C; Similarly, manganese-coated biochar showed removal ability of Sb(III) (0.94 mg g^{-1}) and Sb(V) (0.73 mg g^{-1}) [25]. Specifically, iron and manganese oxides are ideal choices for the modification of BC owing to their good redox ability and rich surface functional groups [26]. The proximity of Mn and Fe oxides on the biochar matrix creates a synergistic system where Mn oxides primarily drive the oxidation of reduced species, and the adjacent Fe oxides efficiently adsorb the resulting oxidized species as well as the pristine species [27]. This cooperative adsorption-oxidation mechanism is expected to be more effective than either component alone for the removal and detoxification of Sb(III). Therefore, in this study, Fe-Mn oxides were used to improve the efficiency of antimony removal from wastewater by modifying wheat straw BC.

Wheat straw BC was utilized as the raw material to prepare Fe–Mn-modified BC (FMBC) composites by an *in situ* impregnation and carbonization method for the removal of Sb(III) from wastewater to solve the problem of environmental pollution. A series of modern techniques, such as X-ray diffraction (XRD), Fourier transform infrared spectroscopy (FTIR), scanning electron microscopy (SEM), transmission electron microscopy (TEM), and X-ray photoelectron spectroscopy (XPS), was used to characterize the adsorbents. Adsorption kinetics, response surface, and isothermal adsorption experiments were carried out to investigate the adsorption of Sb(III). The results of this study provide theoretical support for the adsorption of Sb(III) by FMBC and an effective solution for the removal of Sb(III) from wastewater.

Materials and Methods

Materials

Wheat straw was collected from a certain location in Suzhou (China). Potassium permanganate ($KMnO_4$), ferrous sulfate ($FeSO_4 \cdot 7H_2O$), potassium antimony tartrate ($C_8H_{10}K_2O_{15}Sb_2$), concentrated hydrochloric acid (HCl), thiourea (CH_4N_2S), ascorbic acid ($C_6H_8O_6$),

potassium borohydride (KBH_4), and sodium hydroxide (NaOH) were obtained from Shanghai Titan Technology (China). All chemicals were of analytical reagent grade and used without further purification. Ultrapure water (with resistivity of 18.2 MΩ cm^{-1} at 25°C) was utilized in all experiments.

Synthesis of FMBC Composite

An appropriate amount of wheat straw powder was placed into a tube-furnace porcelain boat, and the tube furnace (China Kejing, OTF-1200X 80) was heated to 600°C at a rate of 5°C/min under a N_2 atmosphere and continuously fired for 2 h. The powder was removed after it cooled down. Afterward, it was repeatedly rinsed and pumped with ultrapure water to make the pH reach approximately 7. Then, it was dried in a vacuum oven at 105°C for 4 h. After cooling, it was taken out and ground through a 100-mesh sieve to finally obtain wheat straw BC [28].

BC (5 g) was weighed (China Lichen, FA2004), immersed in a mixture of $KMnO_4$ (0.24 mol·L^{-1}, 40 mL) and $FeSO_4{\cdot}7H_2O$ (0.18 mol·L^{-1}, 40 mL) for stirring (China Lichen, LC-DMS-Pro), and was dispersed by ultrasonication for 2 h (China Jinnike, JK-100B). Subsequently, the mixture was dried in an oven at 95°C. The dried sample was placed in a tube furnace under a N_2 atmosphere and pyrolyzed at 600°C for 0.5 h. After pyrolysis, the sample was cooled, washed, and placed in a vacuum oven at 80°C (China Jinghong, DHG-9146A) for 24 h. Finally, the cooled sample was milled and sieved through a 100-mesh sieve to obtain the FMBC composite [29].

Physicochemical Characterization

An X-ray Powder Diffractometer (XRD, Rigaku, SmartLab SE) was used to analyze the phase composition of BC and FMBC before and after Sb(III) adsorption. Fourier Transform Infrared (China Gangdong, FTIR-850) was employed to characterize the infrared spectra and monitor changes in surface functional groups of BC and FMBC before and after Sb(III) adsorption. A Scanning Electron Microscope (German Carl Zeiss AG, ZEISS Sigma 300) was utilized to observe the surface morphology and conduct compositional analysis, while a Transmission Electron Microscope (Thermo Fisher Scientific, FEI Talos F200x) was used to investigate the internal structure. X-ray Photoelectron Spectroscopy (Thermo Fisher Scientific, K-Alpha) was used to analyze the elemental composition and chemical states of the surfaces of BC and FMBC before and after Sb(III) adsorption.

Batch Adsorption Experiments

BC or FMBC (0.1 g) was weighed and added to an Erlenmeyer flask containing 100 mL of Sb(III) solution (5 mg·L^{-1}). Triplicate samples were prepared and placed in a thermostatic shaker (China Zhichu, ZQZY-78AE, 25°C, 200 r·min^{-1}) for shaking. Samples were taken at 10, 20, 30, 60, 90, 120, 240, and 480 min. During sampling, 1 mL of the reaction solution was aspirated using a disposable plastic syringe and filtered through a 0.45 μm microporous membrane. All batch adsorption experiments were performed with three parallel samples, and the average values were reported. The filtrate was determined by atomic fluorescence spectrometry, and the adsorption capacity (q_e) of Sb(III) at each time point was calculated according to Equation (1). The pseudo-first-order and pseudo-second-order kinetic equations, as shown in Equations (2-4), respectively, were used to fit the experimental data [30].

Adsorption capacity (q_e) of Sb(III):

$$q_e = \frac{(C_0 - C_e)V}{m} \tag{1}$$

Pseudo-first-order kinetic linear Equation:

$$\ln(q_e - q_t) = \ln q_e - K_1 t \tag{2}$$

Pseudo-second-order kinetic linear Equation:

$$\frac{t}{q_t} = \frac{1}{K_2 q_e^2} + \frac{t}{q_e} \tag{3}$$

Intra-particle diffusion (IPD) [31]:

$$q_t = k_{ip} t^{0.5} + C_i \tag{4}$$

In the above equations, q_t is the concentration of Sb(III) (mg·g^{-1}) at t time, q_e is the concentration of Sb(III) (mg·g^{-1}) at equilibrium time, t is the adsorption time (min), K_1 is the pseudo-first-order kinetic rate constant (g·mg^{-1}·min^{-1}), K_2 is the pseudo-second-order kinetic rate constant (g·mg^{-1}·min^{-1}), C_0 is the initial concentration of the Sb(III) solution (mg·L^{-1}), C_t is the equilibrium concentration of the Sb(III) solution (mg·L^{-1}), V is the volume of the Sb(III) solution (L), and m is the mass of the adsorbent (g). k_{ip} is the intraparticle diffusion rate constant (mg/(g·$min^{0.5}$)), i is the stage of the IPD model, i is 1 or 2; and C_i (mg·g^{-1}) is a constant.

Design and Optimization of Response Surface

In the optimization design of the response surface methodology (RSM), each factor was set at three levels, numbered as (−1, 0, +1) [32]. After the corresponding experiments were completed in accordance with the designed experimental table, the removal rate of each combination was obtained, and the optimal adsorption-condition combination was derived through optimization [33]. Based on the results of preliminary single-factor experiments, this study adopted the central composite experimental design principle of Box–Behnken designs (BBDs) with four factors and three levels to investigate and optimize four factors [34], namely adsorbent dosage

Table 1. Factors and levels in response surface design.

Investigation factors	Levels		
	-1	0	1
Adsorbent dosage ($g \cdot L^{-1}$)	0.5	1.25	2
Initial concentration of Sb(III) ($mg \cdot L^{-1}$)	1	5.5	10
pH	3	7	11
Reaction time (min)	4	22	40

($g \cdot L^{-1}$), initial Sb(III) concentration ($mg \cdot L^{-1}$), solution pH, and reaction time (min), as shown in Table 1.

Isothermal Adsorption Experiment

Thirty milligrams of FMBC was accurately weighed into a 50 mL plastic vial. Four batches of the same vials were prepared, then 30 mL of Sb(III) solutions with initial concentrations of 1, 2, 5, 10, and 20 $mg \cdot L^{-1}$ were added. The four-batch plastic vials were placed in a constant-temperature shaking incubator at temperatures of 5°C, 15°C, 25°C, and 35°C for shaking for 60 min (the rotation speed was 200 $r \cdot min^{-1}$). Three parallel samples were considered for the different experiments. When sampling, a disposable plastic syringe was used to draw 1 mL of the reaction solution and pass it through a 0.45 μm microporous membrane. The filtrate was determined via the atomic fluorescence method. All batch adsorption experiments were performed with three parallel samples, and the average values are reported. The Langmuir and the Freundlich isothermal adsorption equations were used to fit and analyze the isothermal adsorption experimental data. The fitting equations are as follows [35]:

Langmuir linear Equation:

$$\frac{C_e}{q_e} = \frac{C_e}{q_m} + \frac{1}{K_L q_m} \tag{5}$$

Freundlich linear Equation:

$$\lg q_e = \lg K_F + \frac{1}{n} \lg C_e \tag{6}$$

In the above equations, C_e is the concentration of Sb(III) in the solution at equilibrium ($mg \cdot L^{-1}$); q_e is the equilibrium adsorption capacity ($mg \cdot g^{-1}$); q_m is the maximum adsorption capacity fitted by the Langmuir model ($mg \cdot g^{-1}$); K_L is the Langmuir adsorption equilibrium constant ($L \cdot g^{-1}$); K_F is the affinity coefficient in Freundlich fitting; n is the constant, in which $1/n$ can be used to judge the influence of concentration on the adsorption capacity.

Adsorption thermodynamic parameters, namely, Gibbs free energy change (ΔG^0, KJ mol^{-1}), enthalpy change (ΔH^0, KJ mol^{-1}), and entropy change (ΔS^0, KJ mol^{-1} K^{-1}) related to the feasibility and nature of the adsorption process were calculated with the Equations (7-9) [36]:

$$\Delta G^0 = -RT \ln K_d \tag{7}$$

$$\Delta G^0 = \Delta H^0 - T\Delta S^0 \tag{8}$$

$$\ln K_d = \frac{\Delta S^0}{R} - \frac{\Delta H^0}{R} \cdot \frac{1}{T} \tag{9}$$

Where: K_d is the adsorption equilibrium constant, calculated from the slope of the curve drawn by $ln(q_e/C_e)$ versus C_e at different temperatures by determining the intercept when C_e is 0; q_e is the adsorption capacity (μg g^{-1}); C_e is the equilibrium concentration (μg L^{-1}); R is the ideal gas constant, 8.314 J mol^{-1} K^{-1}); T is the thermodynamic temperature (K).

Determination of Sb(III)

The batch experimental water samples were assessed by atomic fluorescence spectrometry (China Jitian, AFS-8220). The specific operation steps are as follows: This study prepared a 100 $\mu g \cdot L^{-1}$ Sb(III) solution using an Sb(III) standard solution (1000 $mg \cdot L^{-1}$), and then five concentration gradients of Sb(III) solutions with concentrations of 4, 8, 12, 16, and 20 $\mu g \cdot L^{-1}$ were prepared in 10 mL small tubes. After 1 mL of reducing agent (5% thiourea and 5% ascorbic acid) was added, the volume was fixed to 10 mL with 5% hydrochloric acid. Finally, the standard curve of Sb(III) (y = $46.6432x - 6.9971$, R^2=0.9993) was measured by atomic

Table 2. Fitting kinetic parameters of Sb(III) on FMBC.

Adsorbent	Pseudo-first-order model			Pseudo-second-order model		
	q_e ($mg \cdot g^{-1}$)	K_1 (min^{-1})	R^2	q_e ($mg \cdot g^{-1}$)	K_2 ($g \cdot mg^{-1} \cdot min^{-1}$)	R^2
FMBC	3.683	0.194	0.988	3.773	0.153	0.993

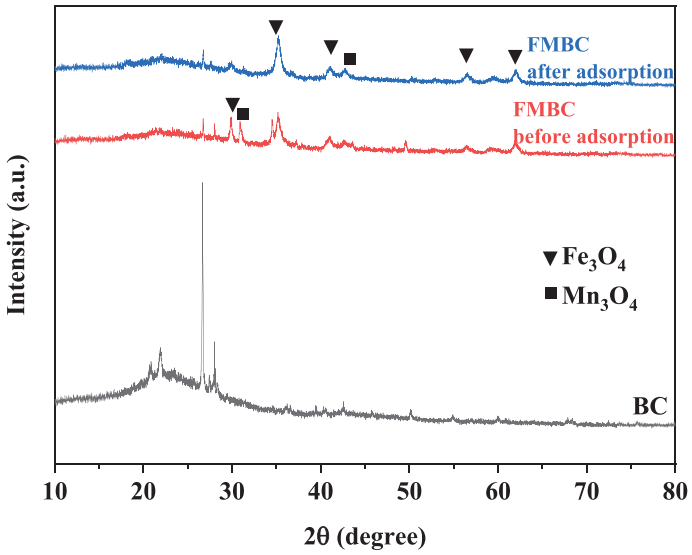

Fig. 1. XRD patterns of BC and FMBC before and after adsorption.

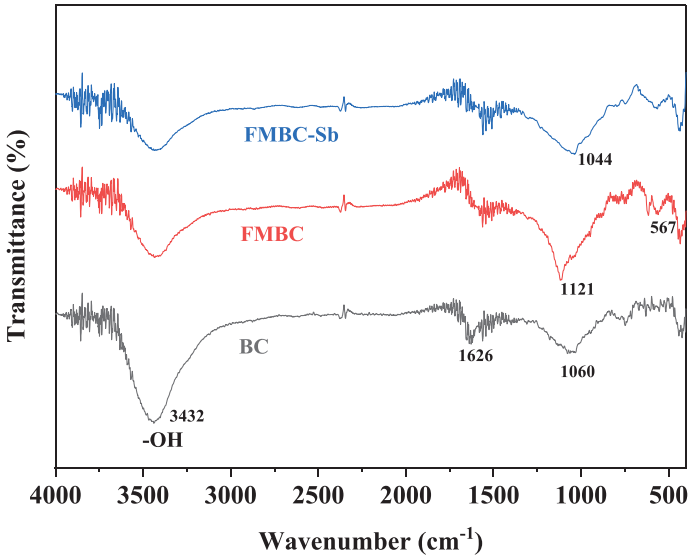

Fig. 2. FTIR spectra of BC and FMBC before and after adsorption.

fluorescence using 5% hydrochloric acid as the carrier solution and a 2% potassium borohydride +0.5% sodium hydroxide solution as the reducing agent. Based on the constructed standard curve, the filtered samples were determined by atomic fluorescence spectrometry. The results obtained were used to calculate the removal rate (P) via the following equation [37]:

$$P = \frac{C_0 - C_t}{C_0} \times 100\% \tag{10}$$

Where P is the Sb(III) removal rate (%), C_0 is the initial concentration of the Sb(III) solution (mg·L^{-1}), and C_t is the equilibrium concentration of the Sb(III) solution (mg·L^{-1}).

Data Analysis

Three parallel samples were set in all experimental groups. The samples were statistically analyzed using SPSS software (P<0.05), and all the graphs were drawn using Origin 2024 software.

Results and Discussion

Adsorbent Characterization

XRD Analysis

The microstructures of the adsorption materials were characterized by XRD patterns, and the results are shown in Fig. 1. The intensities of diffraction peaks

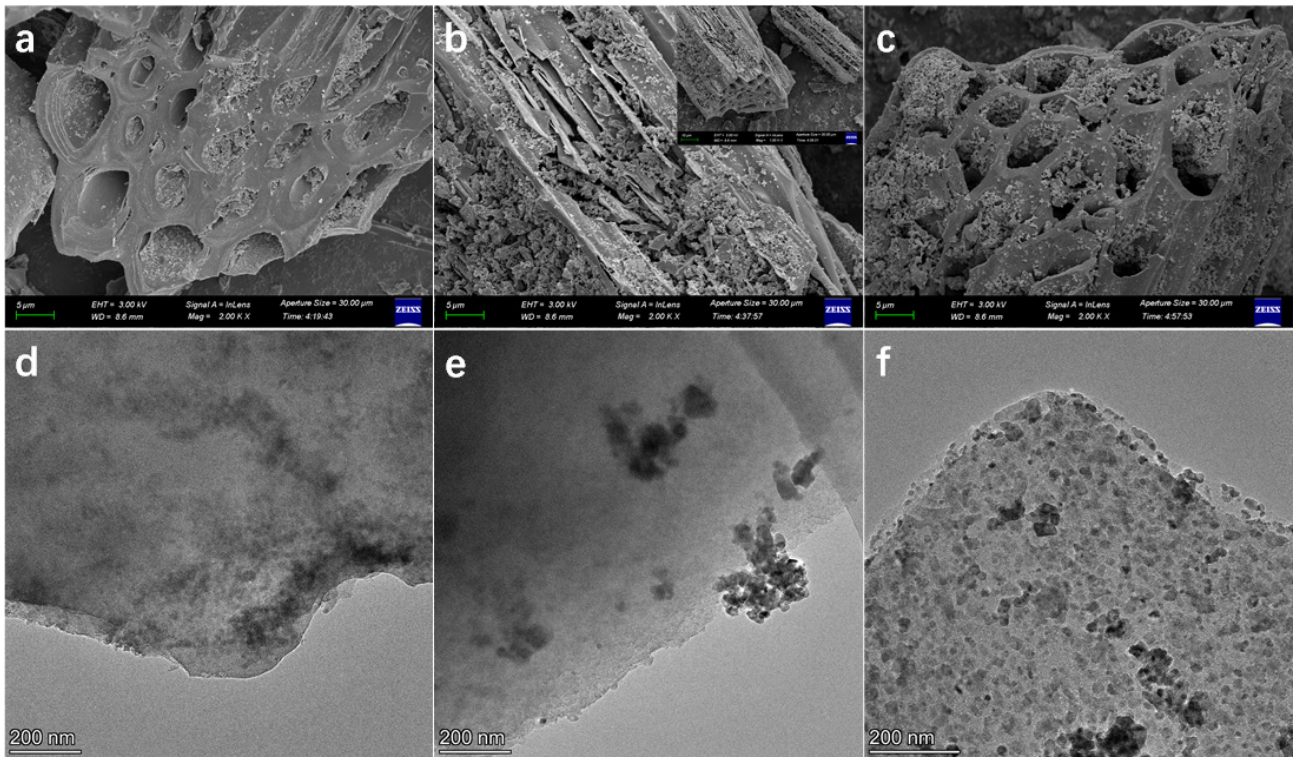

Fig. 3. SEM images (a, b, c) and TEM images (d, e, f) of BC and FMBC before and after adsorption.

corresponding to crystal structures in these samples vary with the 2θ angle [38]. Compared with BC, FMBC exhibits a distinct diffraction peak at approximately 2θ=30°, which corresponds to the crystal structures of Fe_3O_4 (magnetite) and Mn_3O_4 (manganate). However, the lower intensity of this peak indicates that the content of these two crystal structures is relatively low. After the reaction with Sb(III), the intensities of these two crystal structures in FMBC significantly increase, suggesting that Fe_3O_4 and Mn_3O_4 participate in the adsorption of Sb(III).

In addition, the presence of Fe_3O_4 and Mn_3O_4 was detected in FMBC. Among them, iron oxides with multiple valence states are mainly involved in the adsorption process of Sb(III) through complexation and ion exchange, whereas manganese oxides (especially Mn_3O_4 with mixed valence states) play a key role in the oxidation of Sb(III) to Sb(V), which has lower toxicity. XPS analysis shows that the oxidation state of Mn changes after adsorption, and this provides evidence for the aforementioned process.

FTIR Analysis

The changes in surface functional groups of BC and FMBC before and after Sb(III) adsorption were characterized by FTIR, and the results are shown in Fig. 2. As clearly observed from Fig. 2, a prominent characteristic peak appears at approximately 3432 cm^{-1}, which is generated by the bending and stretching vibrations of –OH groups, indicating the presence of carboxylic or phenolic structures [39]. The band at 1626 cm^{-1} is attributed to the stretching vibration of the C=C group. The bands at 1044-1121 cm^{-1} were assigned to the C−O bond of stretching vibration. The vibration peak at approximately 567 cm^{-1} in FMBC belongs to the characteristic peaks of the Fe–O and Mn–O bonds, which is consistent with the XRD analysis results, demonstrating an increase in oxygen-containing functional groups on the BC surface [22, 40]. The increase in oxygen-containing groups on the FMBC surface provides attachment sites for Sb(III) adsorption and enhances the adsorption performance of FMBC for Sb(III). The corresponding changes in the intensity and position of the main peaks before and after adsorption may be due to coordination complexation reactions between Sb(III) and Fe–O/Mn–O bonds.

SEM and TEM

The SEM images of BC before and after Fe–Mn modification are shown in Fig. 3a) and 3b). The surface of BC is slightly rough, with a small number of micropores and a few impurity particles, but no other obvious attachments. The surface of FMBC becomes significantly rougher, with a corresponding increase in the number of micropores. Additionally, numerous Fe–Mn oxide particle clusters of different sizes are loaded onto its surface. Their presence can provide more adsorption sites, endowing FMBC with stronger adsorption capacity. Fig. 3c) shows the SEM morphology of FMBC after Sb adsorption. After the

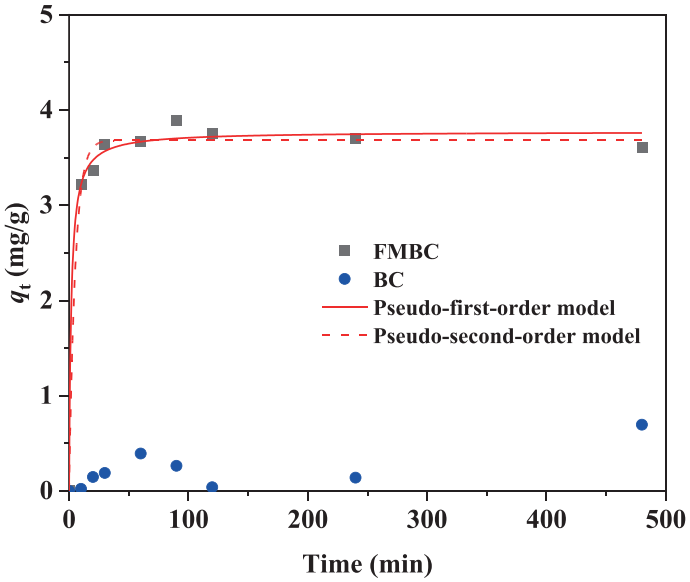

Fig. 4. Effect of contact time on Sb(III) removal by FMBC and BC (Experimental conditions: adsorbent dosage 1.99 g·L^{-1}, initial Sb(III) concentration 1.04 mg·L^{-1}, pH 4.14, temperature 35°C).

adsorption process, FMBC exhibits an overall highly rough surface, with a large number of particle clusters of various shapes distributed in a staggered manner. This irregular distribution of particle clusters increases the contact area between FMBC and the solute. Because of the increased contact area, FMBC can interact more fully with the solute. Therefore, the removal capacity of FMBC toward Sb(III) is significantly improved, enabling it to efficiently remove Sb(III) from the solution and demonstrating excellent adsorption performance [41].

Fig. 3(d-f) show the TEM images of BC, FMBC, and FMBC-Sb, respectively. The surface of BC is smooth, whereas that of FMBC exhibits numerous small particles with an uneven distribution, which increases the specific surface area and adsorption sites, thereby significantly enhancing its performance. The surface of FMBC-Sb also contains many small particles but with a relatively uniform distribution, indicating its unique adsorption performance toward Sb(III).

Adsorption Kinetic Analysis

As shown in Fig. 4, in the 60-min adsorption process, the adsorption capacity of FMBC for Sb(III) gradually increases and eventually stabilizes, indicating that the adsorption reached equilibrium. Under this equilibrium state, the maximum adsorption capacity of FMBC for Sb(III) reaches 3.89 mg·g^{-1}, which is significantly superior to the maximum adsorption capacity of BC for Sb(III) (0.69 mg·g^{-1}).

Additionally, the adsorption process of FMBC was fitted and analyzed using pseudo-first-order, pseudo-second-order, and intraparticle diffusion kinetic models, and the results are presented in Fig. 4 and Tables 2 and 3. The parameter R^2 corresponding to the pseudo-second-order kinetic model for FMBC reaches 0.9925, a value very close to 1. In kinetic fitting analysis, the closer the R^2 value is to 1, the better the model fitting effect is, meaning that the adsorption kinetic process of FMBC is more consistent with the pseudo-second-order kinetic model. The pseudo-second-order kinetic model primarily describes chemical adsorption processes [42]. Generally, the adsorption kinetics follow a two-stage mechanism. The initial phase, marked by a higher k_{1p} value, signifies a fast surface process controlled by the diffusion of molecules to and across the boundary layer. The subsequent phase, with a significantly lower k_{2p} value, marks a transition to a slower regime where the internal diffusion of adsorbate within the particle pores becomes dominant, with significant implications for the overall adsorption rate [43]. However, a negative diffusion rate (k_{2p}) indicates that internal diffusion is virtually absent during the adsorption of Sb(III) by FMBC (Table 3). This characteristic of FMBC indicates that the adsorption mechanism is dominated by chemical adsorption. Furthermore, the FTIR analysis showing

Table 3. Kinetic plots of intraparticle diffusion model parameters of Sb(III) on FMBC.

Adsorbent	Phase	k_{ip} (mg/(g·min$^{0.5}$))	C_i (mg g^{-1})	R_i^2
FMBC	1	0.6841	0.3144	0.9049
	2	-0.005	3.7687	0.0841

Table 4. Box-Behnken response surface experimental design and results.

Test number	Adsorbent dosage ($g \cdot L^{-1}$)	Initial concentration of Sb(III) ($mg \cdot L^{-1}$)	pH	Reaction time (min)	Sb(III) removal rate (%)
1	1.25	1	3	22	85.16
2	2	10	7	22	78.41
3	1.25	10	11	22	59.11
4	2	5.5	11	22	85.21
5	0.5	5.5	11	22	32.22
6	1.25	1	7	4	78.99
7	1.25	10	3	22	80.54
8	1.25	5.5	7	22	71.05
9	0.5	5.5	7	4	30.51
10	0.5	1	7	22	75.64
11	1.25	10	7	40	70.15
12	1.25	1	7	40	87.68
13	2	5.5	3	22	88.25
14	0.5	5.5	3	22	73.90
15	1.25	5.5	3	4	83.93
16	1.25	5.5	11	4	53.71
17	1.25	1	11	22	82.88
18	1.25	5.5	7	22	73.37
19	2	5.5	7	40	86.78
20	2	1	7	22	91.86
21	0.5	5.5	7	40	61.18
22	1.25	5.5	3	40	84.69
23	1.25	10	7	4	50.60
24	2	5.5	7	4	77.62
25	1.25	5.5	7	22	76.22
26	0.5	10	7	22	53.83
27	1.25	5.5	11	40	75.47

an increase in oxygen-containing functional groups suggests that redox reactions may occur in the chemical adsorption process [44].

RSM Analysis

Response Surface Experimental Design and Results

Using BBD, this study obtained 27 experimental combinations by investigating 4 factors, namely, adsorbent dosage, the initial concentration of Sb(III), solution pH, and reaction time [45], as shown in Table 4. Multiple regression modeling was performed using adsorbent dosage, initial Sb(III) concentration, solution pH, and reaction time as independent variables and Sb(III) removal efficiency as the dependent variable to derive the response surface regression equation. The resultant model is expressed as:

$$Y=91.25+2.91A-1.68B-6.41C+0.22D+3.22AC \quad (11)$$

where Y is the Sb(III) removal efficiency (%), A is the adsorbent dosage ($g \cdot L^{-1}$), B is the initial Sb(III) concentration ($mg \cdot L^{-1}$), C is the pH, and D is the reaction time (min).

In the established regression model, F=13.39, P<0.0001, indicating that the regression model reaches an extremely significant level (P<0.01). The coefficient of

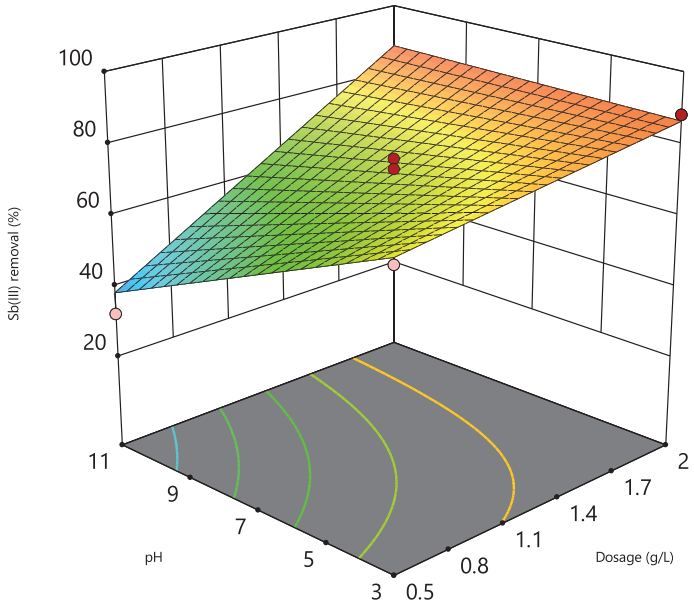

Fig. 5. Interactive effects of adsorbent dosage and pH range on Sb(III) removal efficiency.

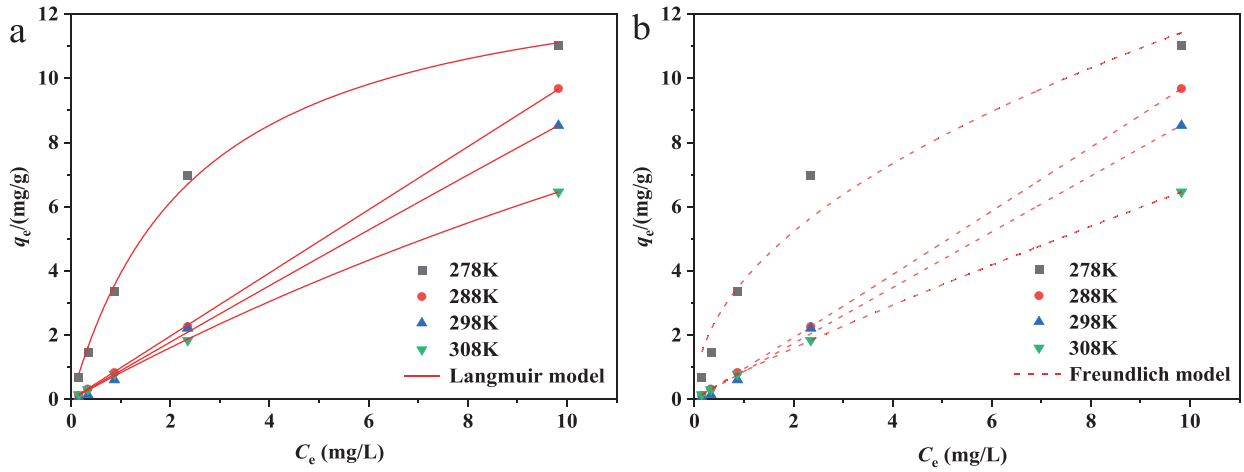

Fig. 6. Effect of initial Sb(III) concentration (0.5-10 mg·L^{-1}) and temperature (278K-308K) on Sb(III) removal by BC and FMBC (Experimental conditions: adsorbent dosage 1.99 g·L^{-1}, pH 4.14).

determination (R^2) is 0.8933, suggesting good agreement between the experimental and actual models [46]. A value of R^2 closer to 1 implies better goodness of fit of the model to the data, meaning smaller discrepancies between the observed and model-predicted values [47]. Based on the above analysis, the model is judged to have a favorable fitting effect and can be used to predict response values.

Response Surface Analysis

Three-dimensional response surface plots can visually reflect the influence of various factors on the response value. The slope of the response surface indicates the degree of influence of two factors on the response value – the steeper the slope, the more significant their interactive effect. As shown in Fig. 5, the removal rate of Sb(III) generally exhibits a downward trend with increasing pH, whereas a lower pH (acidic environment) enhances the Sb(III) removal rate. At lower adsorbent dosages, the change in Sb(III) removal rate is relatively gentle; at higher dosages, the change in removal rate becomes more pronounced. When the pH is 3 and the adsorbent dosage is 2 g·L^{-1}, the maximum Sb(III) removal rate reaches 88.25%. Hence, when the adsorbent dosage is constant, a lower pH leads to a higher Sb(III) removal rate. Conversely, when the pH is constant, a higher adsorbent dosage results in a higher Sb(III) removal rate.

Optimization and Validation of Adsorption Conditions

The optimal combination was obtained through the optimization numerical solution, with the optimal

Table 5. Adsorption isotherm and thermodynamic parameters of Sb(III) on FMBC at 278, 288, 298, and 308K.

T (K)	Langmuir model			Freundlich model			ΔG^0 (kJ mol^{-1})	ΔH^0 (kJ mol^{-1})	ΔS^0 (kJ mol^{-1} K^{-1})
	q_m	K_L	R^2	K_F	n	R^2			
278	13.994	0.391	0.997	3.711	2.033	0.945	–0.924	14.948	0.057
288	13.744	0.443	0.999	3.953	2.126	0.961	–1.766		
298	16.660	0.404	0.981	4.719	2.078	0.996	–1.893		
308	23.762	0.232	0.999	4.324	1.547	0.987	–2.792		

reaction conditions being an adsorbent dosage of 1.99 g·L^{-1}, Sb(III) concentration of 1.04 mg·L^{-1}, pH of 4.14, and reaction time of 4.5 min. Under these conditions, the theoretical Sb(III) removal rate is 93.90%. To verify the accuracy and reliability of the model, three repeated experiments were conducted under the optimal reaction conditions. The experimental results showed that the Sb(III) removal rate reaches 93.73%, which has a small difference from the theoretical value and is consistent with the actual situation, indicating that this study has practical significance.

Adsorption Isotherm Analysis

The Langmuir and the Freundlich adsorption models were fitted and analyzed based on the obtained experimental data, and the fitting results are shown in Fig. 6. From Table 5, the superior fit of the Langmuir model (R^2>0.98) over the Freundlich model across all tested temperatures provides compelling evidence that Sb(III) adsorption on FMBC predominantly follows a monolayer mechanism, suggesting the presence of homogeneous binding sites with uniform energy distribution on the adsorbent surface [48]. The increasing adsorption capacity with temperature, as evidenced by the isotherm data, indicates an endothermic process that may be attributed to several factors, including enhanced dehydration of Sb(III) ions, which facilitates stronger interactions with FMBC's surface functional groups, as well as increased ion mobility and potential thermally induced modifications to the adsorbent's surface chemistry. The Langmuir model's excellent fit implies that FMBC possesses a finite number of specific adsorption sites with high affinity for Sb(III), likely involving chemical interactions such as inner-sphere complexation or ion exchange rather than physical accumulation [49]. This monolayer adsorption behavior is particularly significant for practical applications, as it suggests that FMBC's active sites are highly selective for Sb(III) ions, potentially leading to more efficient removal from aqueous solutions compared to adsorbents exhibiting multilayer adsorption. The temperature-dependent increase in adsorption capacity further indicates that the process may be driven by chemical interactions that require activation energy, consistent with observations in other metal adsorption systems where higher temperatures promote surface complexation reactions [50]. The strong agreement between experimental data and Langmuir model predictions also implies that FMBC's surface sites are energetically equivalent and that intermolecular interactions between adsorbed Sb(III) ions are negligible, which is crucial for predicting adsorption behavior under varying concentration conditions. These findings collectively suggest that FMBC's adsorption mechanism for Sb(III) is likely dominated by specific chemical interactions at well-defined surface sites rather than nonspecific physical adsorption [51], highlighting its potential as a targeted adsorbent for antimony removal from contaminated water sources.

To further elucidate the adsorption behavior of Sb(III) on FMBC, the thermodynamic parameters, including Gibbs free energy change (ΔG^0), enthalpy change (ΔH^0), and entropy change (ΔS^0), were calculated based on the Langmuir model fitting results (Table 5). The negative values of ΔG^0 at all temperatures confirm the spontaneity of the adsorption process, while the positive ΔH^0 (14.948 kJ mol^{-1}) suggests an endothermic nature [52], consistent with the observed increase in adsorption capacity with temperature. This endothermic behavior may arise from the dehydration of Sb(III) ions and the formation of stronger bonds with FMBC's surface sites at higher temperatures. The positive ΔS^0 (0.057 kJ mol^{-1} K^{-1}) indicates increased randomness at the solid-liquid interface during adsorption, likely due to the release of water molecules from hydrated Sb(III) ions and from FMBC surface functional groups.

Mechanism of Sb(III) Adsorption by FMBC

XPS was employed to analyze the elemental composition and valence state changes on the surface of FMBC before and after adsorption to further investigate the adsorption mechanism of Sb(III) by FMBC [30], with the results shown in Fig. 7. Figs. 7(a-c) present the scanning energy spectra of Fe 2p, Mn 2p, and Sb 3d+O 1s on FMBC before and after the reaction, respectively. As indicated in Fig. 7a), the characteristic absorption peaks of Fe(III) appear at binding energies of 725.3 eV and 711.7 eV, while those of Fe(II) are at 723.3 eV and 710.5 eV. Notably, there is almost no obvious change in the valence state of Fe before and after the reaction. The reason is that $FeSO_4 \cdot 7H_2O$ primarily exists as Fe(III) after reacting with $KMnO_4$. In a weakly acidic environment,

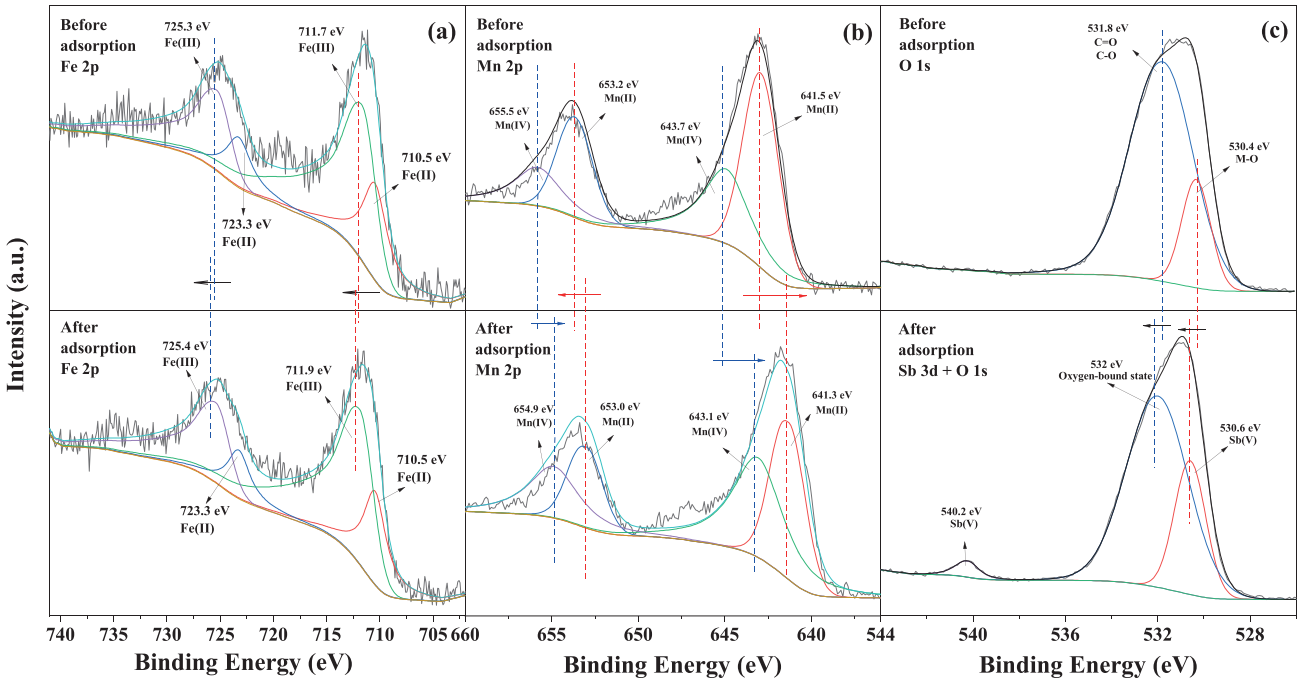

Fig. 7. XPS spectra of Fe *2p* (a), Mn *2p* (b), and Sb *3d*+O *1s* (c) on FMBC before and after reaction.

Sb(III) mainly exists in the form of electrically neutral $Sb(OH)_3$, which undergoes dehydrocondensation with Fe–OH or Mn–OH to form Fe–O–Sb or Mn–O–Sb bonds, accompanied by ion exchange and complexation reactions [53], thereby achieving the removal of Sb(III) [54]. Moreover, before the reaction, the characteristic peaks of Mn(IV) are at 655.5 eV and 643.7 eV, while those of Mn(II) are at 653.2 eV and 641.5 eV. After the reaction, the positions of the characteristic peaks shift significantly, indicating that the change in the valence state of Mn during the adsorption process plays a dominant role in the oxidation of Sb(III). Specifically, Mn(IV) is reduced to Mn(II), and Sb(III) is oxidized to Sb(V), suggesting that a redox reaction occurs during the adsorption of Sb(III) by FMBC [55].

Fig. 7c) shows the deconvolution spectrum of Sb 3d+O 1s. Before the reaction, the O 1s spectral region mainly includes two characteristic peaks at 531.8 eV and 530.4 eV, corresponding to the forms of C=O, C–O, and Mn–O, which are consistent with the FTIR results, indicating the presence of abundant oxygen-containing functional groups. The characteristic peaks of C=O and C–O shift from 531.8 eV to 532 eV before and after the reaction, suggesting that C=O and C–O groups participate in the adsorption of Sb(III). In the Sb 3d spectrum, obvious characteristic peaks of Sb(V) are observed at 540.2 eV and 530.6 eV, indicating that part of Sb(III) is converted into Sb(V) during the adsorption process and binds to the surface sites [56].

The above analyses demonstrate that the adsorption of Sb(III) by FMBC is accompanied by significant oxidation. Functional groups such as –OH, Fe/Mn–O, and Fe/Mn–OH on the surface of FMBC participate in the adsorption process of Sb(III), forming Fe/Mn–O–Sb bonds and undergoing complexation and ion exchange reactions [57].

Conclusions

This study successfully synthesized Fe-Mn modified biochar (FMBC) from wheat straw through in situ impregnation and carbonization. Characterization (XRD, FTIR, XPS) confirmed that Sb(III) removal occurs through redox reactions, complexation, and ion exchange, combining adsorption with detoxification. Under RSM-optimized conditions (1.99 $g \cdot L^{-1}$ dose, 1.04 $mg \cdot L^{-1}$ Sb(III), pH 4.14, 4.5 min contact time), a 93.73% removal rate was achieved. The process follows pseudo-second-order kinetics and Langmuir monolayer adsorption, with a maximum capacity of 23.76 $mg \cdot g^{-1}$ at 35°C. FMBC demonstrates efficient, cost-effective, and sustainable potential for treating antimony-contaminated wastewater.

Acknowledgements

This work was financially supported by the National Natural Science Foundation of China (42207305), the Natural Science Foundation for Excellent Young Scholars of Colleges and Universities in Anhui Province (2024AH030035), the Action Project for Training Young and Middle-Aged Teachers in Anhui Province's Universities (YQZD2024048), the Excellent Academic and Technical Scholars Project of Suzhou University

(2024XJGG12), and the College Students' Innovation and Entrepreneurship Training Program of Anhui Province (S202510379081).

Conflict of Interest

The authors declare no conflict of interest.

References

1. SWAIN C.K. Environmental pollution indices: a review on concentration of heavy metals in air, water, and soil near industrialization and urbanisation. Discover Environment. **2** (1), 5, **2024**.
2. CHEN L., WANG Y., LIU H., ZHOU Y., NIE Z., XIA J., SHU W. Different fates of Sb(III) and Sb(V) during the formation of jarosite mediated by *Acidithiobacillus ferrooxidans*. Journal of Environmental Sciences. **147**, 342, **2025**.
3. FU X., XIE X., CHARLET L., HE J. A review on distribution, biogeochemistry of antimony in water, and its environmental risk. Journal of Hydrology. **625** (part B), 130043, **2023**.
4. LIANG Y.H., LIU Q.C., LI Y.K., LIU F. Speciation Analysis and Ecological Risk Assessment of Antimony in Xikuangshan, Hunan Province. Polish Journal of Environmental Studies. **30** (2), 1289, **2021**.
5. DENG S., REN B., HOU B., DENG R., CHENG S. Antimony-complexed heavy metal wastewater in antimony mining areas: Source, risk and treatment. Environmental Technology & Innovation. **32**, 103355, **2023**.
6. WANG Y., SHAO Q., HUANG S., ZHANG B., XU C. High performance and simultaneous sequestration of Cr(VI) and Sb(III) by sulfidated zerovalent iron. Journal of Cleaner Production. **191**, 436, **2018**.
7. XU D., GAO B., PENG W., GAO L., LI Y. Geochemical and health risk assessments of antimony (Sb) in sediments of the Three Gorges Reservoir in China. Science of the Total Environment. **660**, 1433, **2019**.
8. ADNAN M., XIAO B., ALI M. U., XIAO P., ZHAO P., WANG H., BIBI S. Heavy metals pollution from smelting activities: A threat to soil and groundwater. Ecotoxicology and Environmental Safety. **274**, 116189, **2024**.
9. CARNEIRO M.A., PINTOR A.M., BOAVENTURA R.A., BOTELHO C.M. Arsenic and antimony desorption in water treatment processes: Scaling up challenges with emerging adsorbents. Science of the Total Environment. **929**, 172602, **2024**.
10. BASHIR M.S., RAMZAN N., NAJAM T., ABBAS G., GU X., ARIF M., QASIM M., BASHIR H., SHAH S.S.A., SILLANPÄÄ M. Metallic nanoparticles for catalytic reduction of toxic hexavalent chromium from aqueous medium: A state-of-the-art review. Science of the Total Environment. **829**, 154475, **2022**.
11. ARIF S., ZAFAR S., KHAN M.I., MANZOOR S., SHANABLEH A., GARCIA J.F., HAYAT M. Removal of chromium (VI) by commercial anion exchange membrane BII from an aqueous solution: Adsorption kinetic, equilibrium, and thermodynamic studies. Inorganic Chemistry Communications. **152**, 110696, **2023**.
12. SHANG J., GUO Y., HE D., QU W., TANG Y., ZHOU L., ZHU R. A novel graphene oxide-dicationic ionic liquid composite for Cr(VI) adsorption from aqueous solutions. Journal of Hazardous Materials. **416**, 125706, **2021**.
13. WANG B., WANG Y.L., ZHAO P., WU T., WANG H. Facile and Eco-Friendly Approach to Multifunctional Supramolecular Poly (ionic liquid) Nanoporous Membranes Containing Hydrophilic Anions (Br–, MBr y–, M= Sn, Pb, Sb, Bi). Macromolecules. **57** (10), 5073, **2024**.
14. MA L.Y., LI Q.Y., YU X., JIANG M., XU L. Recent developments in the removal of metal-based engineered nanoparticles from the aquatic environments by adsorption. Chemosphere. **291**, 133089, **2022**.
15. LIANG P., LIU S., LI M., XIONG W., YAO X., XING T., TIAN K. Effective adsorption and removal of Cr(VI) from wastewater using magnetic composites prepared by synergistic effect of polypyrrole and covalent organic frameworks. Separation and Purification Technology. **336**, 126222, **2024**.
16. FU D., KURNIAWAN T.A., WANG Y., ZHOU Z., WEI Q., HU Y., OTHMAN M.H.D., CHEW K.W., GOH H.H., GUI H. Applicability of magnetic biochar derived from Fe-enriched sewage sludge for chromate removal from aqueous solution. Chemical Engineering Science. **281**, 119145, **2023**.
17. VIJAYARAGHAVAN K. Recent advancements in biochar preparation, feedstocks, modification, characterization, and future applications. Environmental Technology Reviews. **8** (1), 47, **2019**.
18. YU X., WANG X., SUN M., LIU H., LIU D., DAI J. Cadmium immobilization in soil using phosphate-modified biochar derived from wheat straw. Science of the Total Environment. **926**, 171614, **2024**.
19. TAN W.T., ZHOU H., TANG S.F., ZENG P., GU J.F., LIAO B.H. Enhancing Cd(II) adsorption on rice straw biochar by modification of iron and manganese oxides. Environmental Pollution. **300**, 118899, **2022**.
20. LESBANI A., PALAPA N.R., SAYERI R.J., TAHER T., HIDAYATI N. High reusability of NiAl LDH/biochar composite in the removal of methylene blue from aqueous solution. Indonesian Journal of Chemistry. **21** (2), 421, **2021**.
21. TRINH A.M.H., LE T.P., TRAN K.A., DO N.H.N., LE K.A., TRAN V.T., LE P.K. Effectiveness of Cobalt-Doped Biochar Derived from Durian Shell for Degradation of Rhodamine B. Indonesian Journal of Chemistry. **25** (2), 420, **2025**.
22. WANG Y.Y., JI H.Y., LU H.H., LIU Y.X., YANG R.Q., HE L.L., YANG S.M. Simultaneous removal of Sb(III) and Cd(II) in water by adsorption onto a $MnFe_2O_4$–biochar nanocomposite. RSC Advances. **8** (6), 3264, **2018**.
23. FANG R., PENG J., YU L., WANG Z., PAN K., YAN C., ZHOU S. Fast preparation of high-performance zero-valent iron biochar materials for the removal of arsenic and antimony pollutants utilizing waste wheat straws. Carbon Neutrality. **4** (1), 14, **2025**.
24. WU A., JIA X., ZHANG K., SHAO J., MAO J., YANG Z., DUAN Z., CHEN W.T., CHANG F., WANG S., HU G. Environmentally friendly zero-valent iron-modified biochar beads for high-performance antimonite removal from aqueous solution. Journal of Cleaner Production. **460**, 142534, **2024**.
25. JIA X., ZHOU J., LIU J., LIU P., WEN B., FENG Y. The antimony sorption and transport mechanisms in the removal experiment by Mn-coated biochar. Science of the Total Environment. 724, 138158, 2020.
26. GONG Y., BAI Y., YE P., LI H. Fast and efficient

remediation of antimony-contaminated surface water and field soil using alumina-supported Fe–Mn binary oxide. Chemosphere. **364**, 143165, **2024**.
27. ZHANG W., QIN S., LI X. Remediation of As(III)-contaminated soil by biochar-loaded Fe-Mn oxides: Remediation efficiency and mechanism. Environmental Research. **270**, 121008, **2025**.
28. EL-HASSANIN A.S., SAMAK M.R., RADWAN S.R., EL-CHAGHABY G.A. Preparation and characterization of biochar from rice straw and its application in soil remediation. Environment and Natural Resources Journal. **18** (3), 283, **2020**.
29. YIN G., SONG X., TAO L., SARKAR B., SARMAH A.K., ZHANG W., LIN Q., XIAO R., LIU Q., WANG H. Novel Fe-Mn binary oxide-biochar as an adsorbent for removing Cd(II) from aqueous solutions. Chemical Engineering Journal. **389**, 124465, **2020**.
30. REVELLAME E.D., FORTELA D.L., SHARP W., HERNANDEZ R., ZAPPI M.E. Adsorption kinetic modeling using pseudo-first order and pseudo-second order rate laws: A review. Cleaner Engineering and Technology. **1**, 100032, **2020**.
31. SUHAIMI N., KOOH M.R.R., LIM C.M., CHAO C.T.C., CHAU Y.F.C., MAHADI A.H., CHIANG H.P., HASSAN N.H.H., THOTAGAMUGE R. The use of gigantochloa bamboo-derived biochar for the removal of methylene blue from aqueous solution. Adsorption Science & Technology. **2022**, 8245797, **2022**.
32. ZUHARA S., MCKAY G. Waste-derived activated carbons for effective adsorptive removal of strontium, barium, and binary pollutants: A response surface methodology study. Journal of Environmental Chemical Engineering. **12** (3), 112836, **2024**.
33. BASHA I.K., ABD EL-MONAEM E.M., KHALIFA R.E., OMER A.M., ELTAWEIL A.S. Sulfonated graphene oxide impregnated cellulose acetate floated beads for adsorption of methylene blue dye: optimization using response surface methodology. Scientific Reports. **12** (1), 9339, **2022**.
34. GHAZALI N.F.H.M., HANAPI N.S.M., ZAINI N., ANIS A.L., MAHMOOD W.M.A.W. Using Box-Behnken Design for Determination of Antimony(III) in Polyethylene Terephthalate by Inductively Coupled Plasma-Optical Emission Spectroscopy. Indonesian Journal of Chemistry. **25** (5), 1514, **2025**.
35. EZZATI R. Derivation of pseudo-first-order, pseudo-second-order and modified pseudo-first-order rate equations from Langmuir and Freundlich isotherms for adsorption. Chemical Engineering Journal. **392**, 123705, **2020**.
36. BHUSHAN D., GUPTA R. Green synthesis and adsorption performance of Eucalyptus globulus leaf modified iron oxide-graphene oxide nanocomposite for Cd(II) and Pb(II) removal from aqueous solution. Environmental Geochemistry and Health. **47** (7), 279, **2025**.
37. FU D., KURNIAWAN T.A., LIN L., LI Y., AVTAR R., OTHMAN M.H.D., LI F. Arsenic removal in aqueous solutions using FeS_2. Journal of Environmental Management. **286**, 112246, **2021**.
38. KHAN H., YERRAMILLI A.S., D'OLIVEIRA A., ALFORD T.L., BOFFITO D.C., PATIENCE G.S. Experimental methods in chemical engineering: X-ray diffraction spectroscopy—XRD. The Canadian Journal of Chemical Engineering. **98** (6), 1255, **2020**.
39. QUAN L., SUN M., QIN C., WANG A., WEN Q., LIU H., SHI L., HU F., ZHOU J., CHEN Y., SHEN Z., XIA Y. Rice husk biochar is more effective in blocking the cadmium and lead accumulation in two Brassica vegetables grown on a contaminated field than sugarcane bagasse biochar. Environmental Geochemistry and Health. **46**, 471, **2024**.
40. LONG X., WANG X., GUO X., HE M. A review of removal technology for antimony in aqueous solution. Journal of Environmental Sciences. **90**, 189, **2020**.
41. TANG S.F., ZHOU H., TAN W.T., HUANG J.G., ZENG P., GU J.F., LIAO B.H. Adsorption characteristics and mechanisms of Fe-Mn oxide modified biochar for Pb(II) in wastewater. International Journal of Environmental Research and Public Health. **19** (14), 8420, **2022**.
42. GUPTA A.D., GIRI B.S., RENE E.R., CHATURVEDI P., GOSWAMI M., SINGH H. Batch and continuous reactor studies for the adsorption of As(III) from wastewater using a hybrid biochar loaded with transition metal oxides: Kinetics and mass transfer analysis. Environmental Engineering Research. **26** (6), 200438, **2021**.
43. XIANG W., ZHANG X., LUO J., LI Y., GUO T., GAO B. Performance of lignin impregnated biochar on tetracycline hydrochloride adsorption: Governing factors and mechanisms. Environmental Research. **215**, 114339, **2022**.
44. DITTMANN D., SAAL L., ZIETZSCHMANN F., MAI M., ALTMANN K., AL-SABBAGH D., SCHUMANN P., RUHL A. S., JEKEL M., BRAUN U. Characterization of activated carbons for water treatment using TGA-FTIR for analysis of oxygen-containing functional groups. Applied Water Science. **12** (8), 203, **2022**.
45. FERREIRA N., VIANA T., HENRIQUES B., TAVARES D.S., JACINTO J., COLONIA J., PINTO J., PEREIRA E. Application of response surface methodology and box–behnken design for the optimization of mercury removal by Ulva sp. Journal of Hazardous Materials. **445**, 130405, **2023**.
46. ZHANG J., WEI Y., LI H., ZENG E.Y., YOU J. Application of Box–Behnken design to optimize multi-sorbent solid phase extraction for trace neonicotinoids in water containing high level of matrix substances. Talanta. **170**, 392, **2017**.
47. KUMARI B., TIWARY R.K., YADAV M., SINGH K.M.P. Nonlinear regression analysis and response surface modeling of Cr(VI) removal from synthetic wastewater by an agro-waste *Cocos Nucifera*: Box-Behnken Design (BBD). International Journal of Phytoremediation. **23** (8), 791, **2021**.
48. ANASTOPOULOS I., KYZAS G.Z. Are the thermodynamic parameters correctly estimated in liquid-phase adsorption phenomena? Journal of Molecular Liquids. **218**, 174, **2016**.
49. WU M., YANG G. Adsorption of Sb(III) and Sb(V) over gibbsite surfaces and regulatory effects of doping. Separation and Purification Technology. **377**, 134387, **2025**.
50. CANPOLAT M., ALTUNKAYNAK Y. Isotherm, kinetic, and thermodynamic studies of adsorption of copper(II) and nickel(II) ions using low-cost treated orange peel from aqueous solutions. Environmental Progress & Sustainable Energy. **44** (1), e14509, **2025**.
51. LI J., CHEN W., WENG X., CHEN Z. The removal of Sb from mine wastewater using biosynthesized Fe-Mn nanoparticles: Function and mechanism. Colloids and Surfaces A: Physicochemical and Engineering Aspects. **692**, 133973, **2024**.
52. LIN T.Y., XIE K.H., WU C.Y., WANG L.Y., LIU C.H., SHU C.C. Removal of anionic dyes from an aqueous

solution by a Polyaniline-modified bioflocculant. Journal of the Taiwan Institute of Chemical Engineers. **177**, 106302, **2025**.
53. HE X., MIN X., LUO X. Efficient removal of antimony (III, V) from contaminated water by amino modification of a zirconium metal–organic framework with mechanism study. Journal of Chemical & Engineering Data. **62** (4), 1519, **2017**.
54. XI J., HE M., WANG K., ZHANG G. Adsorption of antimony (III) on goethite in the presence of competitive anions. Journal of Geochemical Exploration. **132**, 201, **2013**.
55. YANG L., SUN K., LIU T., HUANG C., ZHANG L., ZHOU Y., CHEN K., YAO S., ZHANG Z., ZHAO C. An organic visible-photocatalytic-adsorbence mechanism to high-efficient removal of heavy metal antimony ions. Materials Reports: Energy. **4** (3), 100284, **2024**.
56. NUNDY S., GHOSH A., NATH R., PAUL A., TAHIR A.A., MALLICK T.K. Reduced graphene oxide (rGO) aerogel: Efficient adsorbent for the elimination of antimony (III) and (V) from wastewater. Journal of Hazardous Materials. **420**, 126554, **2021**.
57. LI J., CHEN W., WENG X., CHEN Z. The removal of Sb from mine wastewater using biosynthesized Fe-Mn nanoparticles: Function and mechanism. Colloids and Surfaces A: Physicochemical and Engineering Aspects. **692**, 133973, **2024**.